

Investigating the gas-to-dust ratio in the protoplanetary disk of HD 142527

Kang-Lou SOON¹, Munetake MOMOSE¹, Takayuki MUTO², Takashi TSUKAGOSHI³, Akimasa KATAOKA³, Tomoyuki HANAWA⁴, Misato FUKAGAWA³, Kazuya SAIGO³ and Hiroshi SHIBAI⁵

¹ College of Science, Ibaraki University, 2-1-1 Bunkyo, Mito, Ibaraki 310-8512, Japan

² Division of Liberal Arts, Kogakuin University, 1-24-2 Nishi-Shinjyuku, Shinjyuku-ku, Tokyo 163-8677, Japan

³ National Astronomical Observatory Japan, Osawa 2-21-1, Mitaka, Tokyo 181-8588, Japan

⁴ Center for Frontier Science, Chiba University, 1-33 Yayoi-cho, Inage-ku, Chiba, Chiba 263-8522, Japan

⁵ Department of Earth and Space Science, Graduate School of Science, Osaka University, 1-1, Machikaneyama-cho, Toyonaka, Osaka 560-0043, Japan

*E-mail: munetake.momose.dr@vc.ibaraki.ac.jp

Received (reception date); Accepted (acceptance date)

Abstract

We present ALMA observations of the 98.5 GHz dust continuum and the $^{13}\text{CO } J = 1 - 0$ and $\text{C}^{18}\text{O } J = 1 - 0$ line emissions of the protoplanetary disk associated with HD 142527. The 98.5 GHz continuum shows a strong azimuthal-asymmetric distribution similar to that of the previously reported 336 GHz continuum, with a peak emission in dust concentrated region in the north. The disk is optically thin in both the 98.5 GHz dust continuum and the $\text{C}^{18}\text{O } J = 1 - 0$ emissions. We derive the distributions of gas and dust surface densities, Σ_{g} and Σ_{d} , and the dust spectral opacity index, β , in the disk from ALMA Band 3 and Band 7 data. In the analyses, we assume the local thermodynamic equilibrium and the disk temperature to be equal to the peak brightness temperature of $^{13}\text{CO } J = 3 - 2$ with a continuum emission. The gas-to-dust ratio, G/D , varies azimuthally with a relation $G/D \propto \Sigma_{\text{d}}^{-0.53}$, and β is derived to be ≈ 1 and ≈ 1.7 in the northern and southern regions of the disk, respectively. These results are consistent with

the accumulation of larger dust grains in a higher pressure region. In addition, our results show that the peak Σ_d is located ahead of the peak Σ_g . If the latter corresponds to a vortex of high gas pressure, the results indicate that the dust is trapped ahead of the vortex, as predicted by some theoretical studies.

Key words: protoplanetary disks₁ — stars: individual (HD 142527)₂ — stars: pre-main sequence₃ — submillimeter: planetary systems₄

1 Introduction

Dust particles in protoplanetary disks are the foundations of planet formation (Armitage 2010). In the minimum-mass Solar Nebula model, gas and dust particles are distributed smoothly in a radial direction, with surface densities that follow a piecewise power law (Weidenschilling 1977b; Hayashi 1981). The high angular resolution observations by the Atacama Large Millimeter/submillimeter Array (ALMA), however, revealed complicated morphologies in protoplanetary disks as traced by the dust continuum and molecular line emissions, such as dust-depleted gaps, spiral-arms, and crescent-like distributions (Casassus et al. 2013; van der Marel et al. 2013; Isella et al. 2013; Pérez et al. 2014; ALMA Partnership et al. 2015; van der Marel et al. 2016; Nomura et al. 2016; Boehler et al. 2018; Andrews et al. 2018; Tsukagoshi et al. 2019). These observations also show that the spatial distributions of the gas and dust are not necessarily similar, thus resulting in a gas-to-dust ratio that spatially varies within the disks.

Various mechanisms in protoplanetary disks can lead to a different evolution of the gas and dust and thus result in spatial variation of the gas-to-dust ratio. For example, dust particles can lose their angular momentum due to gas-dust friction and radially drift towards the central star (Weidenschilling 1977a). The gas-dust friction may also result in the settling of larger grains toward the disk midplane (Dominik et al. 2007; Pinte et al. 2016). Dust filtration may also occur at the edges of gaps in the dust that has been cleared by planets, in which smaller particles migrate inward to the disk inner region while larger particles are retained at the edges (Rice et al. 2006). Large-scale high pressure gas vortices can also trap dust particles in the azimuthal direction, which may explain the asymmetric structure observed in some protoplanetary disks (Barge & Sommeria 1995; Klahr & Henning 1997; Birnstiel et al. 2013; Zhu & Baruteau 2016; Baruteau & Zhu 2016). Other mechanisms that can change the gas-to-dust ratio are the growth and fragmentation of dust particles near the snowline (Zhang et al.

2015; Okuzumi et al. 2016), as well as secular gravitational instability (Takahashi & Inutsuka 2014; Takahashi & Inutsuka 2016). In these cases the dust particles tend to accumulate in concentric rings around the star. Gas may also be dispersed from the disk by photoevaporation, creating regions with a low gas-to-dust ratio within several astronomical units of the inner disk, favorable for planet formation (Gorti et al. 2015). The existence of one or several planets can also dramatically alter the gas and dust disk structure (Dipierro et al. 2016; Kanagawa et al. 2016; Dong et al. 2017). While the dominant mechanisms that result in the distribution of the gas-to-dust ratio may differ from disk to disk, the ratio may provide clues concerning the processes that lead to the observed disk structures and is crucial in understanding the back-reaction from dust to gas if the ratio is low (Gonzalez et al. 2017; Dipierro et al. 2018).

HD 142527 is a binary system consisting of two pre-main sequence stars: the primary star HD 142527A and the secondary star HD 142527B. The distance to HD 142527 derived by Arun et al. (2019) based on the *Gaia* observations (Gaia Collaboration et al. 2016; Gaia Collaboration et al. 2016) is $157 \text{ pc} \pm 1 \text{ pc}$. The primary star is a Herbig F6 – F7IIIe (Malfait et al. 1998; van den Ancker et al. 1998) star with a mass of approximately $2.4 M_{\odot}$ and age of 2.96 Myr (Fukagawa et al. 2013; Arun et al. 2019). The secondary star is a M dwarf with a mass of $0.13 M_{\odot}$, which orbits around the primary star at an angular distance of approximately $0''.1$ (Biller et al. 2012; Close et al. 2014; Lacour et al. 2016). The binary system is surrounded by an inner disk close to 30 au and a massive outer disk whose gas content extends to approximately 400 au (Verhoeff et al. 2011; Muto et al. 2015); the inner disk is separated from the outer disk by a dust-depleted region, or gap, that extends to a radius of 150 au. ALMA observations of HCO^+ hint at the existence of gas filaments across this gap, through which the material is funneled from the outer disk to the inner disk (Casassus et al. 2013). The accretion rate is estimated to be $10^{-7} M_{\odot} \text{ yr}^{-1}$ (Mendigutía et al. 2014). Near infrared images show that there are at least six spiral arms in the outer disk (Avenhaus et al. 2014). From the different spatial distribution of emission seen at the near- and mid-infrared wavelengths, the outer disk is thought to be inclined to the line-of-sight, with the northeastern half appearing to be the furthest and the southwestern half the nearest (Fukagawa et al. 2006; Fujiwara et al. 2006). The inclination angle of the outer disk and the position angle of the disk major axis have been derived as 27° and 161° , respectively, from the kinematics traced by the $^{13}\text{CO } J = 3 - 2$ line emission (Fukagawa et al. 2013). On the other hand, the inner disk is modeled to be inclined at 70° relative to the outer disk (Marino et al. 2015). The inner disk shadows the northern and southern regions of the outer disk from stellar irradiation causing a drastic drop in the intensity of infrared wavelengths in the two regions (Avenhaus et al. 2014). At the submillimeter and

longer wavelengths, the dust continuum emission of the outer disk shows a crescent structure in which the northern region is significantly brighter than the southern region (Fukagawa et al. 2013; Casassus et al. 2015). Simulations by Price et al. (2018) show that the observed features of the disk (e.g., spiral arms, cavity, HCO^+ streamers) may be explained by just considering the interaction between the disk and the binary system. Their results also predict that the disk-binary interaction can create the asymmetric dust disk without invoking a gas vortex in the disk northern region (see also Ragusa et al. 2017).

In previous research, Muto et al. (2015) and Boehler et al. (2017) derived the gas and dust surface densities and the gas-to-dust ratio of the outer disk of HD 142527 by modeling ALMA observations at Band 7. This research focused on the northern and southern regions of the outer disk, which correspond to the sectors where the dust continuum emission is brightest and faintest at Band 7, respectively. The gas-to-dust ratio was derived to be ~ 3 and ~ 30 in the northern and southern regions, respectively, and the results indicate that dust is concentrated in the northern region. However, discussions concerning the detailed spatial variations in the gas-to-dust ratio were beyond the scope of these papers as only two regions were studied. Herein, we extend on previous studies by deriving the spatial distribution of the gas-to-dust ratio across the outer disk of HD 142527. We assume the local thermal equilibrium and derive the gas and dust surface densities by using ALMA observations of the ^{13}CO and C^{18}O molecular line and dust continuum emissions, at both Band 3 ($\nu \approx 100$ GHz) and Band 7 ($\nu \approx 330$ GHz).

This paper is organized as follows. In Section 2 we introduce the ALMA Band 3 data as well as the previously published ALMA Band 7 data for the HD 142527 system. In Section 3, we present the calibrated images of the ALMA Band 3 data and compare them to that from Band 7. We describe the methods used to derive the gas and dust surface densities in Section 4 and discuss the results in Section 5. Section 6 provides a summary of our research.

2 Observations and data reduction

We used the ALMA Cycle 2 Band 3¹ and Cycle 0 Band 7² observational data of HD 142527 to investigate the distribution of the gas-to-dust ratio in the disk. The observational details are described in the following subsections.

¹ Project code: ADS/JAO.ALMA#2013.1.00670S

² Project code: ADS/JAO.ALMA#2011.0.00318S

2.1 ALMA band 3 data

Band 3 data were taken at seven execution blocks carried out on the nights of the 4th, 5th, and 15th July 2015. Depending on the block, the bandpass calibrator used was either the J1427–4206 or J1617–5848, while the absolute flux calibrator was either Ceres, Pallas, Titan, or J1427–4206³. The flux of the quasar J1427–4206 at 103.5 GHz was monitored once in every ≈ 20 days from the late June to the early August in 2015, and judging from these results, the flux variation during the observation period should be less than 10%. For all the execution blocks J1604–4228 was used as the phase calibrator. We used CASA pipeline version 4.3.1 to perform the data reduction and calibration, and during the data reduction two blocks were completely discarded for lacking calibration information. After flagging aberrant data, the total on-source integration time was 2.94 hours and the number of 12 m antennas involved were 37 to 40, thereby forming a range of baselines between 25.05 m and 1566.19 m.

The ALMA correlator was configured to store linear XX and YY polarizations in four separate spectral windows. Two spectral windows were optimally configured for the continuum observation with frequencies centered at 97.50 GHz and 99.50 GHz, and both had an effective bandwidth of 1.875 GHz. The other two windows, each having 3840 channels, were centered at 109.78 GHz and 110.19 GHz to target the $J = 1 - 0$ line emission of C^{18}O and ^{13}CO with a spectral resolution of 15.259 kHz ($\Delta v \approx 0.04 \text{ km s}^{-1}$).

We used CASA version 5.1.0 to image the calibrated visibility and combined the two wide band spectral windows to obtain a continuum centered at 98.5 GHz with a total bandwidth of 4 GHz. We then applied the multi-scale CLEAN algorithm with Briggs weighting (robust parameter 0.5) and deconvolution scale parameters of 0 (corresponding to a point source), 1, and 2 times the average beam size. These parameters are constant throughout the imaging process. In order to improve the signal-to-noise ratio, we performed self-calibration to the continuum image as follows. First, we solved the gain phase of the initial CLEAN model for the continuum image starting from a time interval equal to the total time duration of each scan (which is between 2 minutes and 7 minutes) of the target, followed by shorter time intervals in the order of 240 s, 120 s, and 60 s. After every phase calibration, we performed CLEAN to the continuum image to obtain a new model that could be used in the succeeding phase calibration. Once the phase calibration was completed, we solved the gain amplitude of the last phase-calibrated model at a time interval equal to the time duration of each scan. Lastly, we applied the phase-calibrated and gain-calibrated models to the visibility data of

³ The source name for J1427–4206 was designated as J1427–421 by mistake in the execution block of ADS/JAO.ALMA#2013.1.00670S. We use the correct source name in this paper.

the 98.5 GHz continuum and performed final CLEAN to create an image of the continuum. With self-calibration, the resulting noise of the continuum image is lowered by a factor of approximately five, and a root mean square noise level of $\sigma = 9.6 \mu\text{Jy beam}^{-1}$ is reached. The synthesized beam in full width at half maximum (FWHM) of the final image is $0''.54 \times 0''.44$, oriented along P.A. = 78.1° .

Before imaging the $J = 1 - 0$ line emission of ^{13}CO and C^{18}O , we applied the phase and amplitude solutions that were derived from the self-calibration to the visibility data of the continuum to these CO visibility data. We used Briggs weighting and multiscale deconvolution, similar to the continuum imaging. We then smoothed the frequency channels to an equivalent velocity resolution of 0.30 km s^{-1} . The velocity resolution is set at a slightly smaller value than the observed velocity dispersion, which is approximately 0.4 km s^{-1} as shown in figures 3 and 4 of Muto et al. (2015) as well as in figure 3(d) in this paper, to reveal the emission with the best sensitivity. Finally, we applied a CASA task *imsmooth* to smooth the image cubes of ^{13}CO and C^{18}O so that they had the same angular resolution in the 98.5 GHz continuum image, i.e., $0''.54 \times 0''.44$ (P.A. = 78.1°). The noise level is $\sigma = 2.0 \text{ mJy beam}^{-1}$.

We also created a spectral cube of $\Delta v = 0.12 \text{ km s}^{-1}$ for both the ^{13}CO and C^{18}O line emissions to derive their peak brightness temperature. The beam size was also smoothed to match that of the 98.5 GHz continuum image. The noise level is $\sigma = 2.9 \text{ mJy beam}^{-1}$.

2.2 ALMA band 7 data

The observational setup and calibration process of the Band 7 data are described in detail by Fukagawa et al. (2013) and Muto et al. (2015). In this study, we use the calibrated images of the 336 GHz continuum and the ^{13}CO $J = 3 - 2$ and C^{18}O $J = 3 - 2$ lines produced by Muto et al. (2015). The velocity resolution of the line images is 0.12 km s^{-1} . The synthesized beams of the Band 7 images are smaller than that from Band 3, so we applied *imsmooth* to the Band 7 images to obtain a spatial resolution identical to that of the Band 3 images, i.e., a synthesized beam of $0''.54 \times 0''.44$ (P.A. = 78.1°). The resultant noise rms was $150 \mu\text{Jy beam}^{-1}$ for the continuum, and $5.9 \text{ mJy beam}^{-1}$ and $7.5 \text{ mJy beam}^{-1}$ for the ^{13}CO and C^{18}O image cubes, respectively.

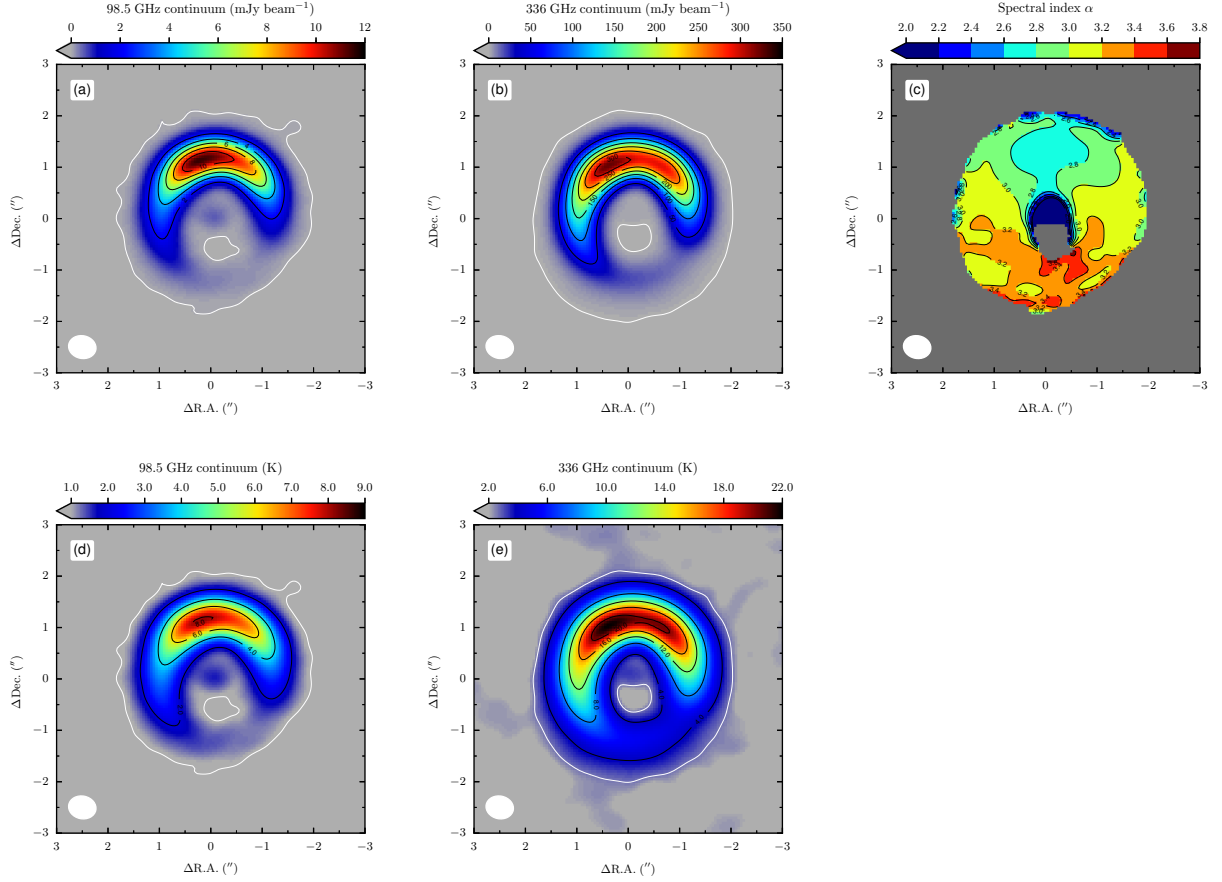


Fig. 1: Images of the 98.5 GHz (left panels) and 336 GHz (middle panels) dust continuum emission; panels (a) and (b) show the emission in units of mJy beam^{-1} , while panels (d) and (e) in units of Kelvin. North is up and east is to the right. The white contours denote the 5σ level, which is $48 \mu\text{Jy beam}^{-1}$ or 0.91 K for the 98.5 GHz images and $750 \mu\text{Jy beam}^{-1}$ or 2.63 K for the 336 GHz images. The spectral index α derived from these dust continuum emission is shown in panel (c). The white ellipse at the bottom left corner indicates the synthesized beam ($0.″54 \times 0.″44$, P.A. = 78.1°).

3 Results

3.1 98.5 GHz continuum emission

The dust continuum emissions of the disk surrounding HD 142527 at 98.5 GHz ($\lambda = 3.0 \text{ mm}$) and 336 GHz ($\lambda = 0.89 \text{ mm}$) are shown in figure 1. The bottom panels in figure 1 present the dust continuum emission in terms of brightness temperature T_B (in units of Kelvin), which was converted from the flux density F_d (in units of mJy beam^{-1}) using the inverse of the Planck function

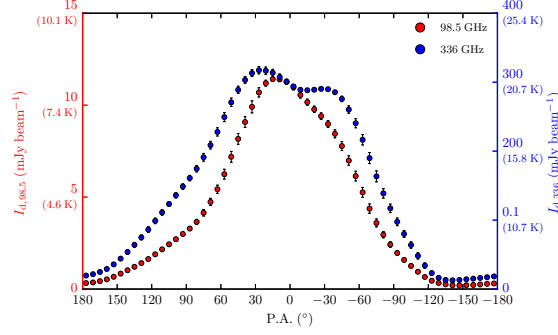


Fig. 2: Dust continuum emission at 98.5 GHz (red plots, left axis) and at 336 GHz (blue plots, right axis) on the ridge plotted as a function of P.A.. The values in the parentheses denote the equivalent brightness temperature derived from the beam size of $0''.54 \times 0''.44$. The error bars denote the standard deviation of the averaged intensity.

Table 1: Maximum and minimum of the 98.5 GHz and the 336 GHz continuum emission along the ridges.

	98.5 GHz		336 GHz	
	Max	Min	Max	Min
Coordinates ($r, \text{P.A.}$) [†]	(1''.1, 15°)	(1''.4, 213°)	(1''.0, 27°)	(1''.2, 219°)
F_d (mJy beam ⁻¹) [‡]	1.14×10	1.96×10^{-1}	3.17×10^2	1.27×10^1
T_B (K) [‡]	8.1	1.2	21.5	4.8
Contrast $\equiv \text{Max/Min}$	58.2		25.0	

[†] The coordinates ($r, \text{P.A.}$) indicate the center of an area of radial size $0''.1$ and angular size 6° .

[‡] The standard deviations (not shown) of flux density F_d and brightness temperature T_B in the area centered at ($r, \text{P.A.}$) are less than 1% of their mean values.

$$T_B = \frac{h\nu}{k} \left[\ln \left(\frac{2h\nu^3}{c^2 F_d / \Omega} + 1 \right) \right]^{-1}, \quad (1)$$

where c , h , and k denote the speed of light, the Planck constant, and the Boltzmann constant, respectively. The solid beam angle Ω is defined as

$$\Omega = \frac{\pi \theta_{\text{maj}} \theta_{\text{min}}}{4 \ln(2)}, \quad (2)$$

where θ_{maj} and θ_{min} are the FWHM of the beam major and minor axes, respectively. The signal-to-noise ratio of the peak continuum flux at 98.5 GHz is 240. The spatially integrated flux at 98.5 GHz, considering only emission above 5σ level, is 72.1 mJy. On the other hand, the integrated flux at 86.3 GHz (equivalent wavelength 3.476 mm) obtained with the Australia

Telescope Compact Array (ATCA) at a coarser beam of $16''.2 \times 2''.9$ is $47.1 \text{ mJy} \pm 6.5 \text{ mJy}$, and the spectral index between $800 \mu\text{m}$ and 3.476 mm is derived to be ≈ 3 (Verhoeff et al. 2011). With this spectral index, the integrated flux at 98.5 GHz corresponds to 48.5 mJy at 86.3 GHz , indicating that the ALMA observation recovers all the flux.

Both 98.5 GHz and 336 GHz continuum images reveal an asymmetric ring-like structure in their emission. The FWHM radial width of the continuum emission from the outer disk is approximately 100 au , which means that the observation beam (linear scale $\approx 76 \text{ au}$) marginally resolves the disk in the radial direction. The 98.5 GHz continuum emission shows a radial extent of approximately 2 arcsec above the 5σ level, and it shares a similar distribution with that observed at 336 GHz , i.e., the outer disk exhibits a crescent-like structure as a result of the concentration of dust in the northern region. Hereafter, we use the word *ridge* to refer to the line that connects the radial peak of a physical quantity in every P.A. direction (as seen from the central star) on the outer disk. To search for the maximum and minimum values along the ridge, the averaged values from an area of radial size $0''.1$ and angular size 6° with coordinates indicated by $(r, \text{P.A.})$ will be used. The maximum and minimum values of the continuum emission along the ridge are listed in Table 1. The contrast of the 98.5 GHz emission along its ridge is approximately 58 and is higher than that at 336 GHz , which is 25 (see also Fukagawa et al. 2013). This difference is because of the lower optical depth at 98.5 GHz ; the optical depth at 336 GHz in the northern region of the disk is $\gtrsim 1$, hence its emission is saturated (Casassus et al. 2015). The lower optical depth at 98.5 GHz also accounts for the lower peak T_{B} , i.e., 8.1 K , compared to 21.5 K at 336 GHz .

The spectral index α is defined as

$$\alpha \equiv \log \left[\frac{F_{\text{d},336}}{F_{\text{d},98.5}} \right] / \log \left[\frac{336 \text{ GHz}}{98.5 \text{ GHz}} \right], \quad (3)$$

and is shown in figure 1(c). The index varies smoothly in the azimuthal direction; in the northern region $\alpha \approx 2.8$, while in the southern region $\alpha \approx 3.4$. When the Rayleigh-Jeans approximation is valid, the flux density is proportional to $\nu^{2+\beta}$, where β is the dust opacity spectral index. The smaller value of α might indicate a smaller β (Beckwith et al. 1990; Beckwith & Sargent 1991; Miyake & Nakagawa 1993), but the spectral slope also gets flatter as the optical depth at 336 GHz gets higher. We will derive β and optical depth from the dust continuum images at 98 GHz and 336 GHz in Section 4.1.

Figure 2 shows the flux density of the continuum emission on the ridge as a function of P.A.. A dip in intensity at P.A. $\sim 0^\circ$ is seen at 336 GHz , rendering the emission morphology to be a double-peaked structure; however, there is no dip at the same P.A. direction at 98.5 GHz .

The 336 GHz emission is so opaque that it would be more sensitive to dust temperature than dust surface density; the dip may therefore reflect a temperature drop in the disk atmosphere (Casassus et al. 2015). In fact, the intensity at infrared wavelengths is also lower at P.A. $\sim 0^\circ$ (as well as at P.A. $\sim 160^\circ$, see Avenhaus et al. 2014) and is thought to be the result of a shadow from a warped inner disk (Marino et al. 2015). On the other hand, the 98.5 GHz emission is optically thin and should also depend on the dust surface density; here, the shadow is not apparent.

3.2 $^{13}\text{CO } J = 1 - 0$ line emission

Figure 3 displays the moment maps of the $^{13}\text{CO } J = 1 - 0$ line emission. The moment maps are created by applying a Keplerian masking and a noise masking to the channel maps (see Appendix 1).

Compared to the 98.5 GHz continuum emission, the ^{13}CO 0th-moment is observed to have a wider radial extent of approximately 3 arcsec and is more axisymmetric. The contrast between the north and the south is approximately 1.4; the ridge in the 0th-moment map has a maximum at $(0''.8, 33^\circ)$ where the integrated intensity is $F_{\text{int}} = 71.1 \text{ mJy beam}^{-1} \text{ km s}^{-1}$ and a minimum at $(1''.0, 213^\circ)$ where $F_{\text{int}} = 49.5 \text{ mJy beam}^{-1} \text{ km s}^{-1}$. In the northern region, the ridge of the 0th-moment is located inwards of that associated with the continuum emission, which is owing to the higher optical depth of the ^{13}CO line.

Figures 4(a) and (c) show the peak T_{B} of the $^{13}\text{CO } J = 1 - 0$ line spectrum; as mentioned in Section 2, these maps are created from the image cube of the velocity resolution of 0.12 km s^{-1} . Figure 4(a) shows the peak T_{B} of the line emission after subtracting the continuum level; the continuum level is estimated from the line free channels of the spectral window containing the ^{13}CO line emission, which is centered at 110.2 GHz and is denoted by black contours in the maps. This continuum emission has a total bandwidth of 54 MHz. On the other hand, figure 4(c) shows the peak T_{B} of ^{13}CO including the 110.2 GHz continuum emission. The continuum-subtracted peak T_{B} in figure 4(a) shows a dip in the northern region where the dust continuum emission is brightest. This is similar to the $J = 3 - 2$ line emission of ^{12}CO , ^{13}CO (figure 4b), and C^{18}O (figure 6b) (Fukagawa et al. 2013; Perez et al. 2015; Boehler et al. 2017), as well as that of $\text{HCN } J = 4 - 3$ and $\text{CS } J = 7 - 6$ (van der Plas et al. 2014). As discussed by Weaver et al. (2018), the dip is due to a high optical depth of dust continuum and/or molecular line emission. The peak T_{B} of ^{13}CO with the continuum emission included, shown in figure 4(d), has a higher brightness temperature in the north and there is no dip observed at the peak

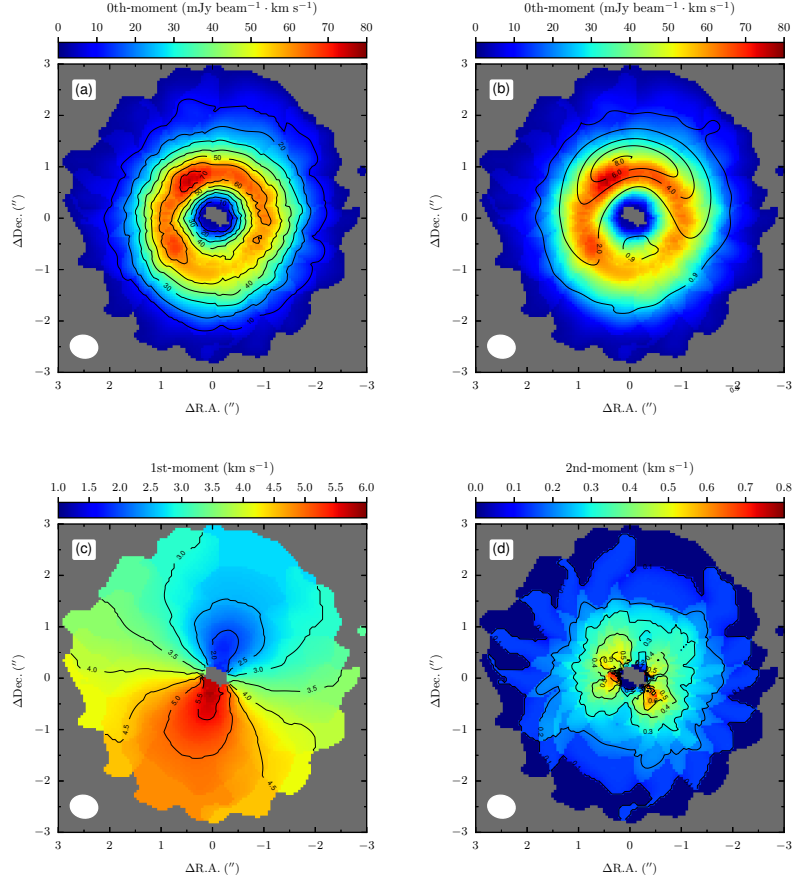


Fig. 3: Moment maps of the $^{13}\text{CO } J = 1 - 0$ line emission created from the image cube of spectral resolution $\Delta v = 0.30 \text{ km s}^{-1}$. The white ellipse in the left bottom corner indicates the synthesized beam, which is identical to that of the 98.5 GHz continuum image ($0''.54 \times 0''.44$, P.A. = 78.1°). The moment maps are created from velocity channels in the range of $v_{\text{lsr}} = 1.2 \text{ km s}^{-1} - 6.3 \text{ km s}^{-1}$ (see Appendix 1) after applying a Keplerian mask in the channels and then clipping emissions lower than 3.5σ ($\sigma = 2.0 \text{ mJy beam}^{-1}$). In panel (b), the 98.5 GHz continuum emission shown in figure 1(d) are superimposed as contours on the 0th-moment image.

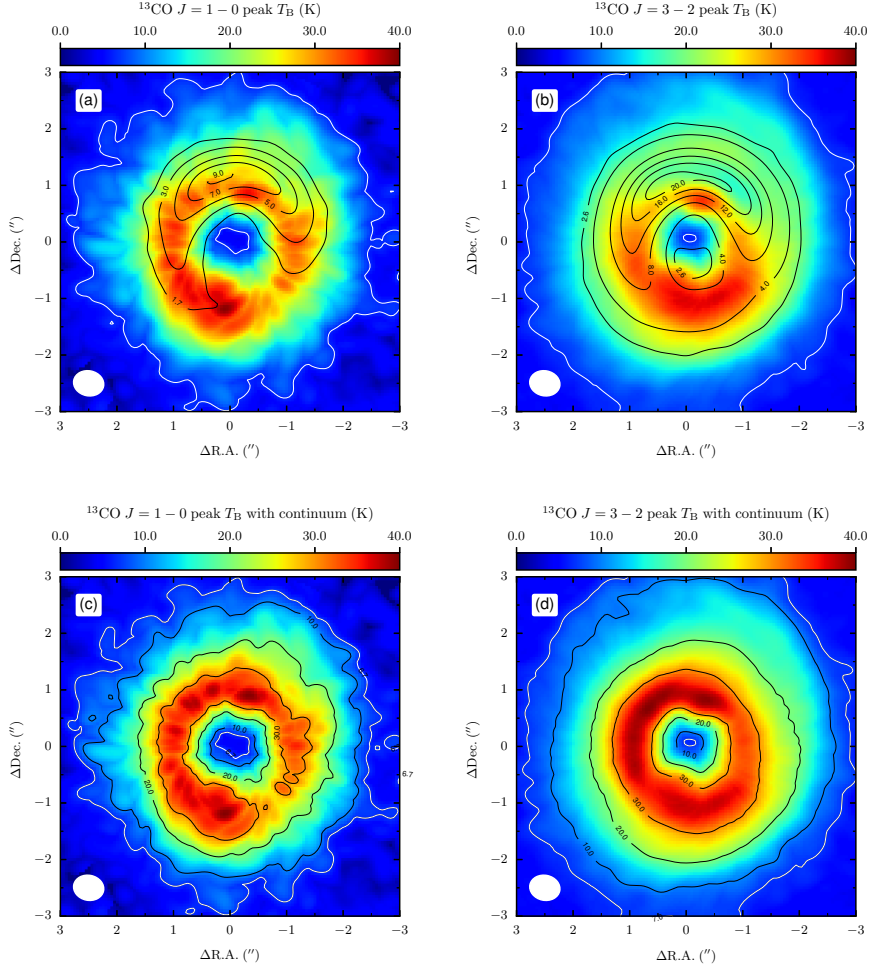


Fig. 4: Peak surface brightness of ^{13}CO ; the left and right panels show the peak T_B of the $J=1-0$ and $J=3-2$ line emission, respectively. The maps in the top row are the peak T_B after subtracting the continuum. The black contours in panel (a) denote the narrow-band continuum emission (see text for details), while those in panel (b) denote the 336 GHz continuum emission as shown in figure 1(d). The maps in the bottom row are the peak T_B with the continuum emission. In panels (a) and (c), the white contours denote the 3.5σ level, which are 6.56 K and 6.74 K, respectively. In panels (b) and (d), the white contours denote the 5σ level, which are 6.91 K and 6.97 K, respectively.

of the continuum emission. In each P.A. direction, the peak T_B of $^{13}\text{CO } J=1-0$ with the continuum included (figure 4c) is in the range of $T_B = (26 - 40)$ K; it is similar to that of the $^{13}\text{CO } J=3-2$ (figure 4d), implying that both lines are optically thick at the center of the line. An exception is seen in the region of P.A. = $200^\circ - 240^\circ$ where the peak T_B of $^{13}\text{CO } J=1-0$ with continuum emission drops to $T_B \approx 26$ K, compared to that of $^{13}\text{CO } J=3-2$, which is

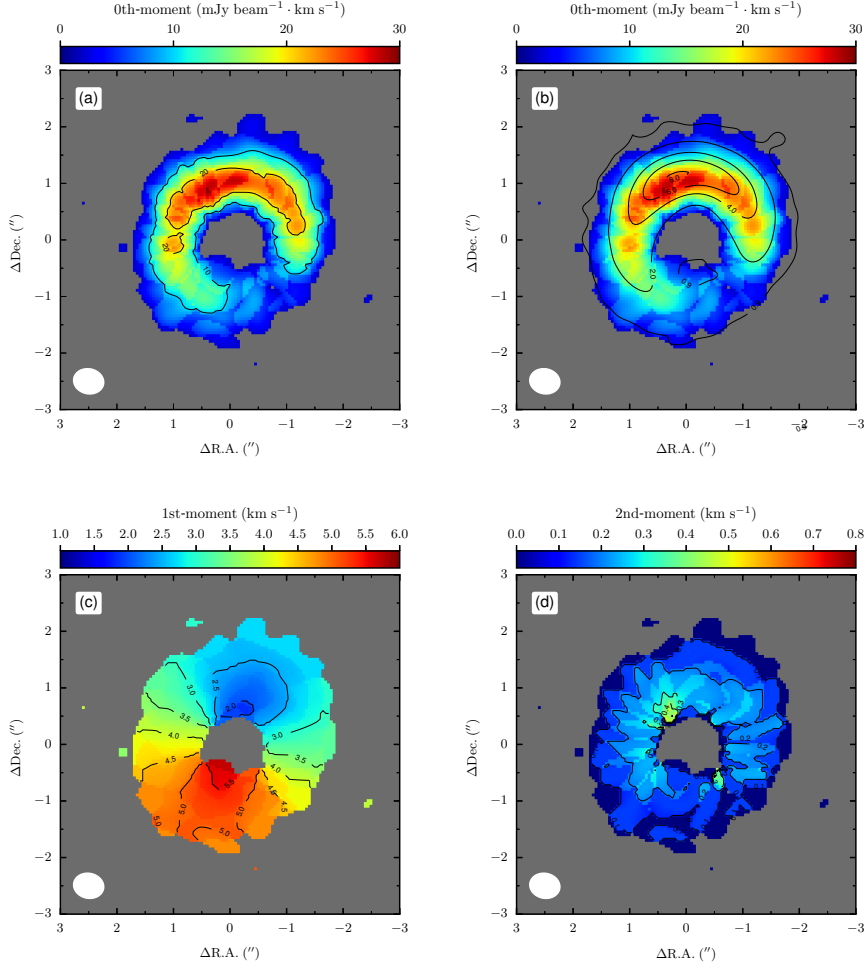


Fig. 5: Similar to figure 3, for the $\text{C}^{18}\text{O } J = 1 - 0$ line emission. The spectral resolution is $\Delta v = 0.30 \text{ km s}^{-1}$. The synthesized beam has the same size and shape as that of the 98.5 GHz continuum image ($0''.54 \times 0''.44$, P.A. = 78.1°). The moment maps are created from velocity channels in the range of $v_{\text{lsr}} = (1.5 - 5.7) \text{ km s}^{-1}$ (see Appendix 1), after applying a Keplerian mask in the channels and then clipping emissions lower than 3.5σ ($\sigma = 2.9 \text{ mJy beam}^{-1}$).

$T_{\text{B}} \approx 36 \text{ K}$, suggesting that the $J = 1 - 0$ line emission in this region is optically thin.

3.3 $\text{C}^{18}\text{O } J = 1 - 0$ line emission

Figure 5 displays the moment maps of the $\text{C}^{18}\text{O } J = 1 - 0$ line emission created with the same Keplerian masking and noise masking as those of $^{13}\text{CO } J = 1 - 0$ shown in figure 3. Compared to that of ^{13}CO , the C^{18}O is confined in a narrower radial extent of $r \approx 0''.5 - 2''.0$. This is because of the weaker emission of $\text{C}^{18}\text{O } J = 1 - 0$. In the southwestern region of P.A. = $180^\circ - 240^\circ$, the emission is much weaker and is below 10σ .

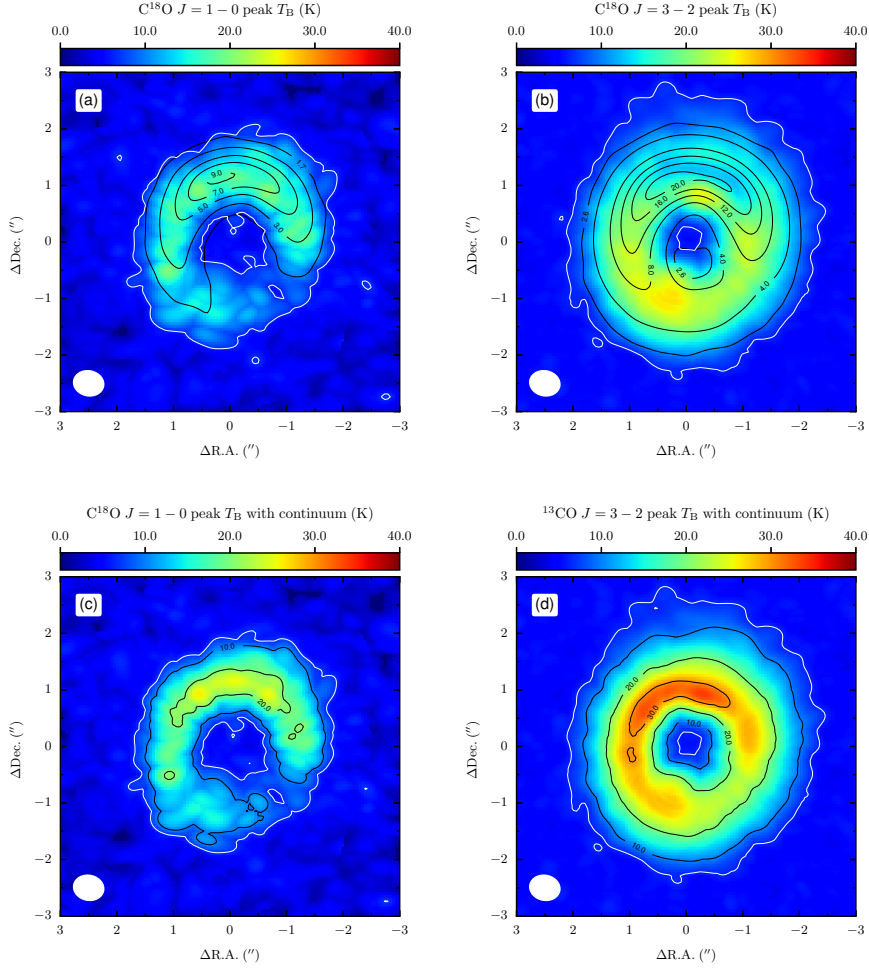


Fig. 6: Similar to figure 4, for the C^{18}O $J = 1 - 0$ (left panels) and $J = 3 - 2$ (right panels) line emission. The black contours in panel (a) denote the narrow-band continuum emission centered at the rest frequencies of the $J = 1 - 0$ line emission (see text for details), while those in panel (b) denote the 336 GHz continuum emission as shown in figure 1(d). In panels (a) and (c), the white contours denote the 3.5σ level, which are 6.53 K and 6.70 K, respectively. In panels (b) and (d), the white contours denote the 5σ level, which are 6.32 K and 6.38 K, respectively.

The peak of the 0th-moment in figure 5(a) is located at $(0''.9, 27^\circ)$, close to the continuum peak with $F_{\text{int}} = 28.7 \text{ mJy beam}^{-1} \text{ km s}^{-1}$. The ridge of 0th-moment is lowest at $(0''.9, 225^\circ)$ where $F_{\text{int}} = 6.95 \text{ mJy beam}^{-1} \text{ km s}^{-1}$. The contrast of the ridge is thus 4.13.

Figure 6(a) shows the peak surface brightness of the C^{18}O $J = 1 - 0$, while figure 6(c) shows the peak T_{B} with the continuum emission. The continuum emission in figure 6(a) is centered at 109.8 GHz with a bandwidth of 54 MHz, created using the same method as that

shown in figure 4(a). The surface brightness of $\text{C}^{18}\text{O } J = 1 - 0$ with continuum emission is significantly weaker than that of the $^{13}\text{CO } J = 1 - 0$ and $J = 3 - 2$, as well as that of the $\text{C}^{18}\text{O } J = 3 - 2$ shown in figures 6(b) and (d), indicating that the $\text{C}^{18}\text{O } J = 1 - 0$ is optically thin. The peak T_{B} is ≈ 25 K in the north while it is ≈ 10 K in the south, and its distribution is similar to that of the continuum emission.

4 Analyses

In this section, we derived the gas and dust surface density for the disk of HD 142527 under the assumptions of local thermodynamic equilibrium (LTE). We do not consider dust sedimentation at the midplane and assume that the gas and dust are well-mixed in the disk. We assume the physical temperatures of the gas and dust, T_{d} and T_{g} , to be identical. These temperatures are taken from the peak T_{B} of $^{13}\text{CO } J = 3 - 2$ including the continuum emission, as shown in figure 4(d); this temperature is referred to as the disk temperature in the following. Since the $^{13}\text{CO } J = 3 - 2$ emission in the disk inner region is optically thin and does not reflect the physical temperature, in the following analyses we mask out the inner region in which the brightness temperature is less than 30 K. Due to the disk inclination, the western region of the disk (P.A. = $161^\circ - 341^\circ$) is closest to us while the eastern region is the furthest from us. The disk temperature at the far side is higher by about 3 K, since the surface of the disk that is irradiated by the central star is exposed to us. The disk is assumed to be isothermal in a vertical direction. A model where T_{d} is assumed to be 80% of T_{g} is discussed in Appendix 2.

4.1 Derivation of dust surface density

The dust surface density is derived from $\Sigma_{\text{d}} = \tau_{\text{d}}/\kappa_{\text{d}}$, where τ_{d} is the optical depth of the dust continuum emission and κ_{d} is the dust opacity. We first calculate τ_{d} at 98.5 GHz and 336 GHz from the radiative transfer equation

$$I_{\text{d}} = [B_{\nu}(T_{\text{d}}) - B_{\nu}(T_{\text{bg}})] [1 - \exp(-\tau_{\text{d}})], \quad (4)$$

where I_{d} denotes the intensity of the continuum emission, B_{ν} is the Planck function, $T_{\text{bg}} = 2.7$ K the temperature of the cosmic background radiation. The results are shown in figures 7(a) and (b). The peak τ_{d} at 98.5 GHz is 0.24 and is co-spatial to its peak continuum emission. On the other hand, peak τ_{d} at 336 GHz is 0.82, and is located at the western component of the double-peaked structure seen at the 336 GHz emission; this is due to the lower disk temperature at the near side. The dust opacity is highly uncertain and depends on the particle compositions,

structures, as well as size distributions (Miyake & Nakagawa 1993; Draine 2006; Kataoka et al. 2014; Birnstiel et al. 2018); in the analyses, we adopt the canonical dust opacity (per dust mass) κ_d described by Beckwith et al. (1990),

$$\kappa_d = 10 \left(\frac{\nu}{10^{12} \text{ Hz}} \right)^\beta \text{ cm}^2 \text{ g}^{-1}, \quad (5)$$

where β is the dust opacity spectral index and is calculated from the τ_d distributions via

$$\beta = \log \left[\frac{\tau_{d,336}}{\tau_{d,98.5}} \right] / \log \left[\frac{336 \text{ GHz}}{98.5 \text{ GHz}} \right] \quad (6)$$

and shown in figure 7(c). The opacity index varies throughout the disk; in the southern region, β is close to the interstellar value of 1.7 (Planck Collaboration et al. 2014), while in the northern region, it is ≈ 1 . The β in the north can be interpreted as the consequence of the growth of dust grains and is qualitatively consistent with the modeling results based on polarization observations (Ohashi et al. 2018). Dust scattering can strongly depend on the dust compositions and structures (Tazaki et al. 2016; Tazaki & Tanaka 2018), but we have ignored it in this study. This is because the observed intensity does not depend strongly on the dust scattering if the scattering opacity is comparable to the absorption opacity, and the modeling of the dust continuum map shows that this is the case in the lopsided disk around HD 142527 (Soon et al. 2017; Boehler et al. 2017).

Figure 8(a) shows the derived dust surface density Σ_d . Along the ridge of Σ_d , the maximum is located at $(1''.2, 315^\circ)$ where $\Sigma_d = 3.08 \times 10^{-1} \text{ g cm}^{-2}$ and the minimum is located at $(1''.2, 225^\circ)$ where $\Sigma_d = 9.14 \times 10^{-3} \text{ g cm}^{-2}$. The derived spatial location of the peak Σ_d does not correspond to that of the peak continuum emission at 98.5 GHz which is optically thin; this is mainly due to the lower temperature in the near side of the disk as well as the β distribution. Similarly, because of the temperature and β distributions, the derived Σ_d ridge contrast of 33 is lower than that of the 98.5 GHz continuum emission, which is 58.

Boehler et al. (2017) successfully reproduce the dust continuum observations at 342 GHz in P.A. = $16^\circ - 26^\circ$ (north P.A. sector) and P.A. = $216^\circ - 226^\circ$ (south P.A. sector) using a disk model, in which the peak dust surface densities are 0.65 g cm^{-2} in the north sector and 0.012 g cm^{-2} in the south sector (see Figure 13 and Table 1 of their paper). Their modeling is based on the ALMA observations with a beam of $0''.26 \times 0''.21$. By convolving the models of dust surface density derived by Boehler et al. (2017) with the beam size of our ALMA observations (i.e., $0''.54 \times 0''.44$, P.A. = 78.1°), the peak dust surface densities in the north and south P.A. sectors are derived to be $\approx 0.4 \text{ g cm}^{-2}$ and $\approx 0.006 \text{ g cm}^{-2}$, respectively. After correcting for

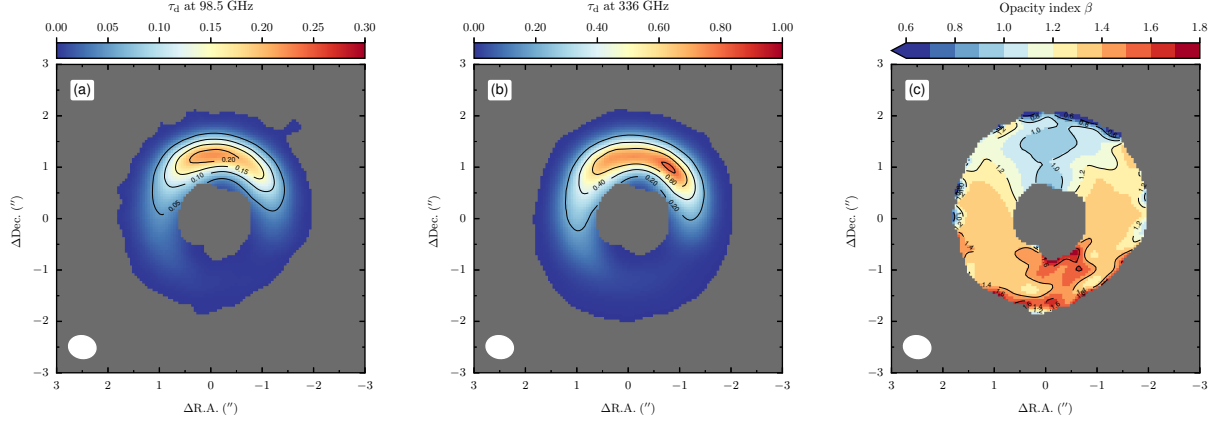


Fig. 7: Optical depth τ_d of the (a) 98.5 GHz and (b) 336 GHz continuum emission. Dust spectral opacity index β derived from Equation (6) is shown in panel (c).

the difference in dust opacity⁴, these correspond to $\approx 0.3 \text{ g cm}^{-2}$ and $\approx 0.009 \text{ g cm}^{-2}$. While our results in the south P.A. sector agrees with Boehler et al. (2017), our results for the north P.A. sector, i.e., $\Sigma_d \approx 0.2 \text{ g cm}^{-2}$, is approximately 70% of that derived by Boehler et al. (2017). This inconsistency may be due to the high optical depth of the dust continuum in the northern regions; the inherent uncertainty in the estimate on Σ_d is large (Soon et al. 2017). Furthermore, omitting the dust scattering may underestimate Σ_d , and hence the Σ_d ridge contrast (Soon et al. 2017; Birnstiel et al. 2018).

4.2 Derivation of gas surface density

We derived the disk H_2 gas surface density Σ_g from the $J = 1 - 0$ and $J = 3 - 2$ line emission of C^{18}O by assuming the interstellar abundance $\chi(\text{C}^{18}\text{O}/\text{H}_2) = 1.79 \times 10^{-7}$ (Wilson 1999); the validity of the abundance is discussed in Section 5.3. The $J = 3 - 2$ emission is used for the derivation of Σ_g in the region of P.A. = $180^\circ - 240^\circ$, where the $J = 1 - 0$ emission is weak.

The optical depth of the molecular line τ_g in the velocity channels is calculated from the radiative transfer equation, which is similar to Equation (4) but takes the form

$$I_g = [B_\nu(T_g) - B_\nu(T_{\text{bg}})] [1 - \exp(-\tau_g)] \exp(-\tau_d), \quad (7)$$

i.e., the factor $\exp(-\tau_d)$ is included to account for the line emission absorbed by the dust. Here, τ_d is the optical depth of the narrow-band continuum emission at 109.8 GHz, which is shown as contours in figure 6(a), in the case of the C^{18}O $J = 1 - 0$ line emission. When the above

⁴ Boehler et al. (2017) use a constant dust absorption opacity of 2.9 g cm^{-2} . The dust opacity κ_d used in this study are $\approx 3.4 \text{ g cm}^{-2}$ and $\approx 2.0 \text{ g cm}^{-2}$ in the north and south P.A. sectors, respectively.

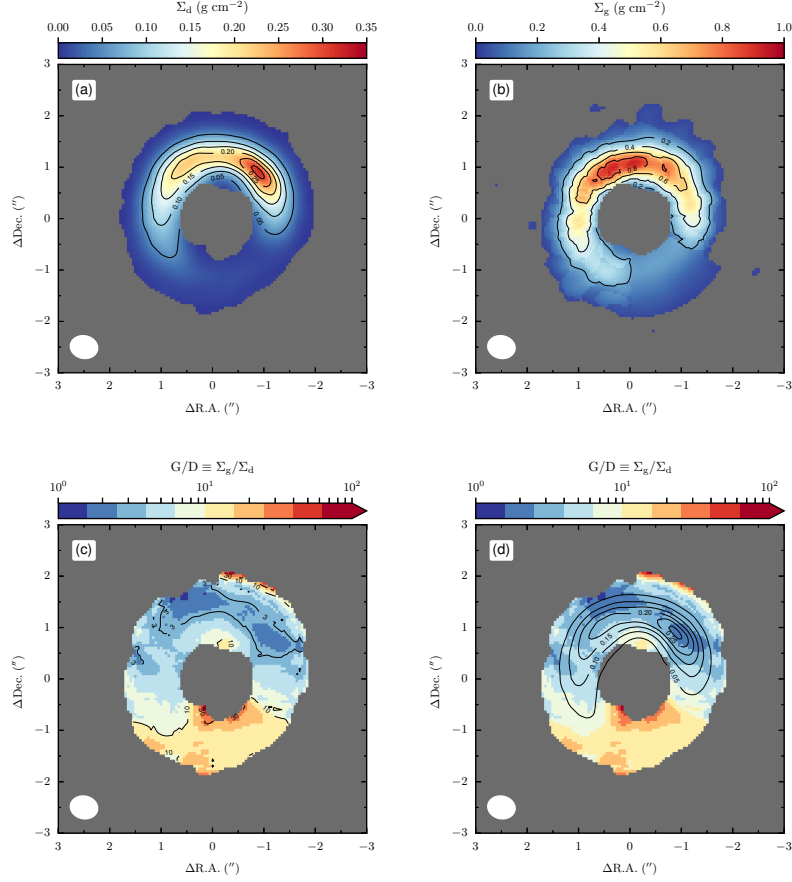


Fig. 8: Derived results of (a) dust surface density Σ_d , (b) gas surface density Σ_g , and (c) gas-to-dust ratio $G/D \equiv \Sigma_g/\Sigma_d$. In panel (d) the contours of Σ_d in panel (a) are superimposed on the G/D image.

equation is applied to the $\text{C}^{18}\text{O } J = 3 - 2$ line emission, on the other hand, τ_d refers to the 336 GHz continuum emission, i.e., the continuum image in figure 1(b). The optical depth τ_g is related to the total (particle number) column density N_{tot} of the CO isotopologue by

$$N_{\text{tot}} = \frac{3h}{8\pi^3\mu^2 J_u} \left(\frac{kT_{\text{ex}}}{hB_0} + \frac{1}{3} \right) \exp\left(\frac{E_{J_u}}{kT_{\text{ex}}}\right) \times \left[\exp\left(\frac{h\nu}{kT_{\text{ex}}}\right) - 1 \right]^{-1} \sum [\tau_g(v)\Delta v] \quad \text{cm}^{-2}, \quad (8)$$

where μ , J_u , and B_0 , are the dipole moment, the rotational quantum number of the line transition upper level, and the rigid rotor rotational constant, respectively (Mangum & Shirley 2015). The excitation temperature T_{ex} is equal to T_g in the LTE analysis. The gas surface density is then calculated by $\Sigma_g = m_{\text{H}_2} N_{\text{tot}}/\chi$, where m_{H_2} is the molecular mass of H_2 .

Figure 8(b) shows the derived results of Σ_g . At P.A. = 180° and P.A. = 240° , the surface

density derived from the $\text{C}^{18}\text{O } J = 1 - 0$ and $\text{C}^{18}\text{O } J = 3 - 2$ lines differs by less than 10%, indicating a smooth variation of Σ_g derived from the two lines. Along the ridge of Σ_g , the maximum is located at $(1''.0, 3^\circ)$ where $\Sigma_g = 9.14 \times 10^{-1} \text{ g cm}^{-2}$, while the minimum is located at $(1''.0, 189^\circ)$ where $\Sigma_g = 1.75 \times 10^{-1} \text{ g cm}^{-2}$. The contrast between the two directions is approximately 5, similar to the contrast of the $\text{C}^{18}\text{O } J = 1 - 0$ 0th-moment ridge. Boehler et al. (2017) derived the peak gas surface density to be 1.125 g cm^{-2} and 0.3 g cm^{-2} in the north and south P.A. sectors, respectively. Similar to the beam convolution performed to the model dust surface density in discussed in Section 4.1, after convolving the model gas surface density derived by Boehler et al. (2017) with our observations beam size the peaks are derived to be $\approx 1.0 \text{ g cm}^{-2}$ and $\approx 0.2 \text{ g cm}^{-2}$. Our results are thus consistent with those derived by Boehler et al. (2017).

Along the ridge of $^{13}\text{CO } J = 1 - 0$ 0th-moment in P.A. = $200^\circ - 240^\circ$, τ_g can also be solved from Equation (7). Within this P.A. and the radial range $r = 0''.6 - 1''.6$, the column density derived from the $^{13}\text{CO } J = 1 - 0$ and $\text{C}^{18}\text{O } J = 3 - 2$ line emission are $N_{\text{tot}}(^{13}\text{CO}) = (1.98 \pm 0.21) \times 10^{19} \text{ cm}^{-2}$ and $N_{\text{tot}}(\text{C}^{18}\text{O}) = (1.98 \pm 0.12) \times 10^{18} \text{ cm}^{-2}$, respectively; the uncertainties only include the propagation of 1σ noise level. The ratio $N_{\text{tot}}(^{13}\text{CO})/N_{\text{tot}}(\text{C}^{18}\text{O})$ is derived to be 9.99 ± 1.67 , and it agrees with the value of the local interstellar medium (8.1 ± 1.1) within the uncertainty (Wilson 1999).

5 Discussions

5.1 G/D and correlation between gas and dust surface densities

Figure 8(c) shows the G/D, defined as the ratio of Σ_g to Σ_d ; figure 10(c) shows the same results in polar coordinates. The estimated G/D is ~ 3 and ~ 20 in the northern and southern regions, respectively, and G/D gradually varies along the azimuthal direction. Our results are consistent with the modeling results by Muto et al. (2015) and Boehler et al. (2017), but they only focused on two sectors centered at P.A. = 21° and P.A. = 221° . We successfully derived the projected G/D distribution across the disk and found that G/D in the outer disk varies along the azimuthal direction. The low G/D in the northern region may be important in the formation of planetesimals (Lambrechts & Johansen 2012; Raettig et al. 2015). Two-dimensional simulations predicted that a vortex would be destroyed by the dust back reaction when G/D got low (Fu et al. 2014), but succeeding three-dimensional simulations have shown that this effect disappears (Lyra et al. 2018).

Figure 9(a) shows the relation between Σ_g and Σ_d on the dust ridge, where the peak T_B

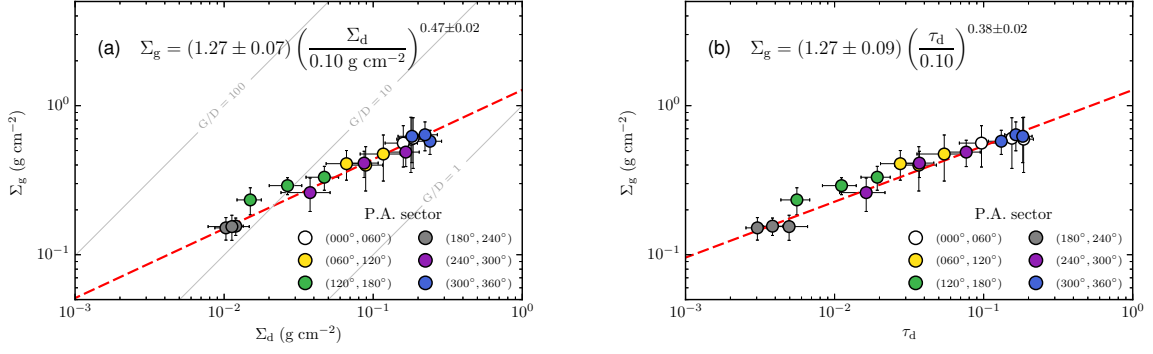


Fig. 9: Panel (a) shows the correlation between the gas surface density Σ_g and the dust surface density Σ_d ; the gray lines indicate the gas-to-dust ratio of $G/D = 1, 10, 100$. Panel (b) shows the correlation between Σ_g and the dust optical depth at 98.5 GHz, τ_d . The best-fit power law of exponent p is drawn as red dashed line. In both panels, the data points are averaged values in a bin of angular size 20° and radial size $0''.5$, and the error bars indicate the standard deviation of the values in the bin. The colors of the data points denote the P.A. of the points.

of $^{13}\text{CO } J = 3 - 2$ is highest, and the estimate of the temperature is most reliable. The plot can be fitted by a power law for which the exponent p (indicated in the top left corner of the plots) is $p = 0.47$. The relation $\Sigma_g \propto \Sigma_d^p$ corresponds to $G/D \propto \Sigma_d^{p-1}$, and therefore figure 9(a) suggests that G/D varies approximately with $\propto \Sigma_d^{-0.53}$. This relation may be a critical test for future theoretical studies to understand the trapping efficiency of dust grains and the origin of the asymmetric disk structure around HD 142527.

Figure 9(b) is similar to figure 9(a), but with the horizontal axis replaced by the dust optical depth at 98.5 GHz. Again, we use a power law and obtain the best fit exponent $p = 0.38$. The exponent in this case is smaller than that of the relation shown in figure 9(a), since there is an azimuthal variation of β (or κ_d) as shown in figure 7(c).

5.2 Relative spatial distribution of gas and dust surface densities

Figure 10 compares the spatial distributions of Σ_g and Σ_d in the polar coordinates. From figures 3(c), 5(c), and the infrared images (Fujiwara et al. 2006), the disk is thought to be rotating in a clockwise rotation. Comparing figures 10(a) and 10(b), we see that the peak Σ_d is located at P.A. $\approx 315^\circ$, which is downstream of the peak Σ_g located at P.A. $\approx 3^\circ$. If the northern region of high Σ_g corresponds to a vortex with higher pressure, then the dust will accumulate at a region shifted ahead of the vortex. This picture is consistent with the theoretical prediction by Baruteau & Zhu (2016) if the Stokes number, St , of the dust particles is $\gtrsim 1$; we estimate the

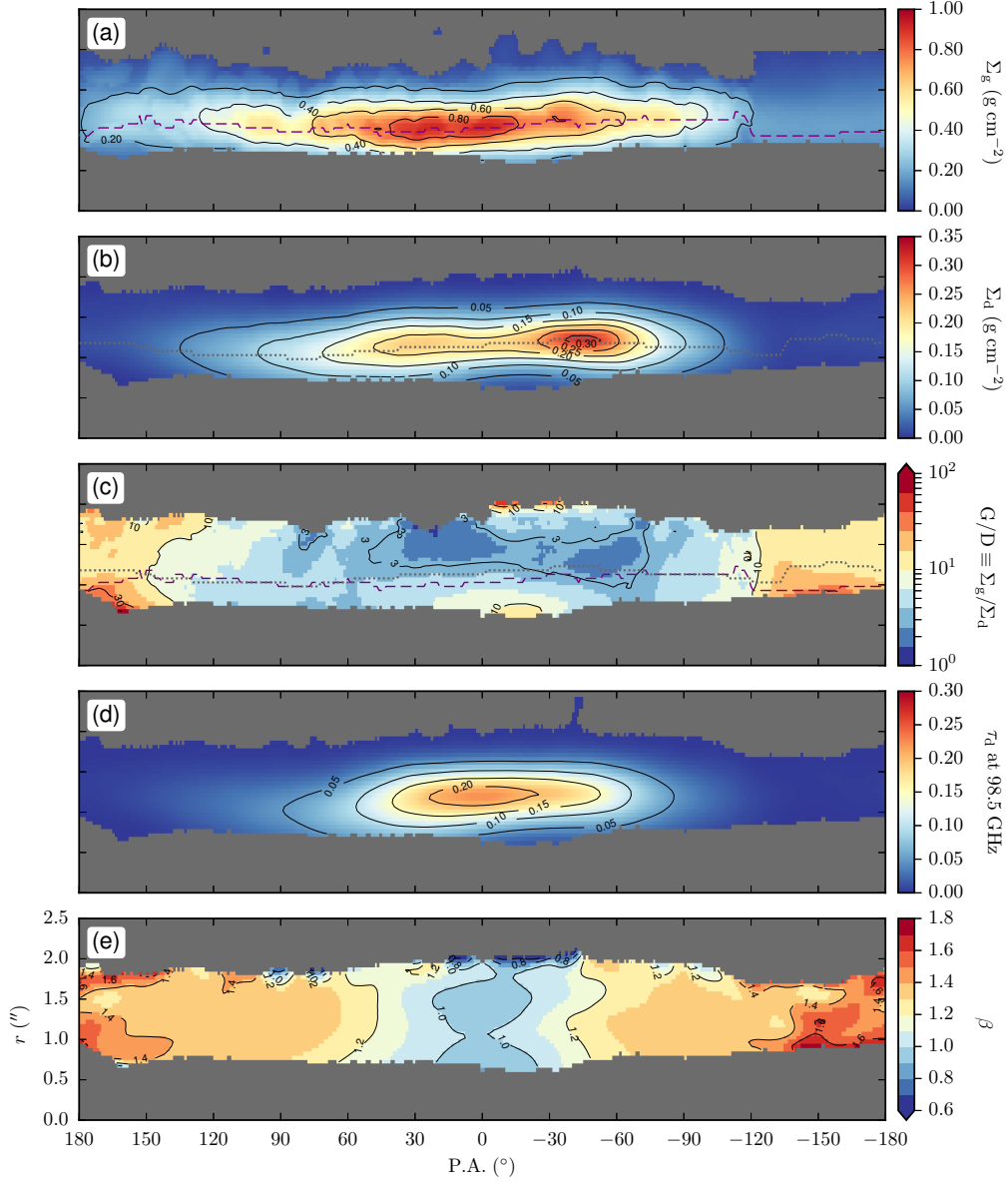


Fig. 10: Derived results of (a) gas surface density Σ_g , (b) dust surface density Σ_d , (c) gas-to-dust ratio G/D , (d) dust optical depth at 98.5 GHz, and (e) dust opacity spectral index β plotted in polar coordinates. The purple dashed line and the gray dotted line in panels (a) and (b) denote the Σ_g and Σ_d ridges, which are also superimposed on the G/D map in panel (c).

physical radius of the dust particle s by using equation (1) in the paper by the same authors, i.e.,

$$s \approx 4.67 \times \left(\frac{\text{St}}{1}\right) \left(\frac{\rho_{\text{pc}}}{1 \text{ g cm}^{-3}}\right)^{-1} \left(\frac{\Sigma_{\text{g}}}{0.7 \text{ g cm}^{-2}}\right) \text{ mm}, \quad (9)$$

where ρ_{pc} is the internal mass density of the particles. The gas surface density is $\Sigma_{\text{g}} \approx 0.7 \text{ g cm}^{-2}$ where Σ_{d} peaks, and by assuming that $\rho_{\text{pc}} = 1 \text{ g cm}^{-3}$, $s \gtrsim 5 \text{ mm}$ if $\text{St} \gtrsim 1$.

If the lower β in the north indicates a particle growth, $\beta \approx 1$ implies a particle size of $\approx 1 \text{ mm} - 10 \text{ mm}$, and it agrees with the above size estimation. In addition, the estimated size is also consistent with the continuum observations at 34 GHz which should be dominated by thermal emission from particles of size $\sim 1 \text{ mm}$; at 34 GHz one of two clumps of concentrated dust is observed at P.A. $\approx 330^\circ$ (the other is at P.A. $\approx 15^\circ$, Casassus et al. 2015). On the other hand, the dust size estimated here is larger than the estimated size of $150 \mu\text{m}$ based on polarization modeling (Ohashi et al. 2018). One possible explanation to the discrepancy is a segregation of dust size in the disk vertical direction, such that smaller particles (efficient scatterers) float at the upper atmosphere while larger particles (efficient emitters) sediment at the midplane.

Figure 10(d) shows the dust optical depth at 98.5 GHz, τ_{d} , at polar coordinates. Comparing figures 10(a) and 10(d), we see that the peaks of τ_{d} and Σ_{g} share a similar spatial location in the north, which is contrary to the relative distributions of the peaks of Σ_{d} and Σ_{g} . We caution that the derivation of Σ_{d} is highly dependent on κ_{d} , and in this paper we derived Σ_{d} using a κ_{d} whose spatial variation is determined by the β distribution. As shown in Appendix 3, our derived parameters of the dust disk can also reproduce the intensity distributions of the continuum emission at 700 GHz reported by Casassus et al. (2015). To better disentangle κ_{d} and Σ_{d} , however, radiative transfer modeling of a wider frequency range may be required, and this is beyond the scope of this study.

The observations of asymmetric protoplanetary disk around HD 135444B reveal a frequency dependent azimuthal shift in the peak continuum position, which can be interpreted as a consequence of size segregation of dust grains trapped by a vortex (Cazzoletti et al. 2018). Comparing figure 1(a) and (b) (see also Table 1), there is also an azimuthal offset between the 98.5 GHz and 336 GHz peaks in the north. The peak shift in the case of HD 142527, however, may not be due to the size segregation since the 336 GHz emission is fairly optically thick. In fact, the β distribution in the outer disk shown in figure 10(e) is nearly mirror symmetric with respect to P.A. $= 0^\circ$, and there is no gradient along the azimuthal direction from upstream to downstream indicative of dust size segregation. The dynamic range of the observed frequencies

in this study may be insufficient to discuss size segregation in the disk (cf. Casassus et al. 2015).

5.3 Effects of uncertainties in CO abundance

In a protoplanetary disk, the abundance of CO as relative to H_2 can be lower than that in the interstellar medium if CO is depleted due to freeze-out onto dust grains. In addition, CO can also be depleted by photodissociation in the disk upper layer by UV radiation (Miotello et al. 2014; Miotello et al. 2016; Miotello et al. 2017). In fact, the gas masses of several T Tauri disks derived from the HD $J = 1 - 0$ transition, which are considered to be a reliable mass tracer, are found to be a factor of five greater than the masses derived independently from the CO observations without accounting for these CO depleting processes (Bergin et al. 2013; McClure et al. 2016).

Here, we discuss the effects of CO freeze-out and photodissociation in the outer disk HD 142527. CO freeze-out occurs in the disk midplane where the disk temperature is lower than the CO freeze-out temperature, i.e., approximately 20 K (Qi et al. 2011). The disk models used by Muto et al. (2015) show that the temperature in the outer disk of HD 142527 varies radially, and in the disk midplane the temperature is mostly higher than 20 K (see Figure 8 of their paper), implying that the CO freeze-out may be insignificant. On the other hand, the photodissociation is subject to self-shielding and therefore the process is isotope-selective. The less abundant isotopologue will have a thicker photodissociation layer, and the relative abundances among CO, ^{13}CO , and C^{18}O are thus expected to be varying spatially (Shimajiri et al. 2014). In Section 4.2 we derived $N_{\text{tot}}(^{13}\text{CO})/N_{\text{tot}}(\text{C}^{18}\text{O})$ to be similar to the ^{13}CO to C^{18}O ratio in the local interstellar medium; these results might suggest that isotope-selective photodissociation is insignificant in the case of HD 142527. The abundances of these isotopologues relative to CO, however, are still currently unknown and therefore further investigation is required to confirm the photodissociation of CO.

Even if the effects of freeze-out and isotope-selective photodissociation are small, the abundance of CO relative to H_2 still remains uncertain if carbon is locked up in other form of molecules. The detail thermochemical models show that the mass conversion from CO to H_2 would be underestimated by a factor of about three to eight (Yu et al. 2016; Yu et al. 2017; Molyarova et al. 2017). The depletion of more than a factor of ten, however, is unlikely because the gas disk would be gravitationally unstable (Fukagawa et al. 2013). In short, though Σ_{g} , G/D , and the dust size estimated from equation (9) may be underestimated, the exponent

$p \approx 0.5$ found in the power law relation between Σ_g and Σ_d remains valid because p does not depend on the absolute values of Σ_g and Σ_d .

6 Summary

We present the ALMA Band 3 observations of the 98.5 GHz dust continuum and the ^{13}CO $J = 1 - 0$ and C^{18}O $J = 1 - 0$ lines of the protoplanetary disk associated with HD 142527 at a spatial resolution of $\sim 0''.5$, and compare the results to the ALMA observations at Band 7. The 98.5 GHz continuum and C^{18}O $J = 1 - 0$ is optically thin, and we derived the gas-to-dust ratio, G/D, of the outer disk. The main conclusions are as follows.

1. The 98.5 GHz dust continuum shows a similar distribution to that at 336 GHz, where the northern region is brighter than the southern region. The contrast of the 98.5 GHz along its ridge is approximately 58. The spectral index α is ≈ 2.8 and ≈ 3.4 in the northern and southern regions, respectively.
2. The integrated intensity of the ^{13}CO $J = 1 - 0$ line emission is more axisymmetric compared to the dust continuum emission, where the northern region is brighter than the south by a factor of ~ 1.4 . The C^{18}O $J = 1 - 0$ emission is confined in a narrower radial extent, where its peak emission is located near to the 98.5 GHz dust continuum peak; the integrated intensity of the line in the northern region is brighter than the south by a factor of 4.
3. The dust opacity spectral index β is derived to be ≈ 1 and ≈ 1.7 in the northern and southern regions of the disk, respectively; the difference in β between the two regions indicate the difference in dust properties. We use the $J = 1 - 0$ and $J = 3 - 2$ lines of C^{18}O and the 98.5 GHz and 336 GHz continuum emission to derive the disk gas and dust surface densities, Σ_g and Σ_d . We assume the local thermodynamic equilibrium, the interstellar abundance $\chi(\text{C}^{18}\text{O}/\text{H}_2) = 1.79 \times 10^{-7}$, and the canonical dust opacity described by Beckwith et al. (1990) by varying β spatially. The derived surface densities are $\Sigma_g \sim 0.9 \text{ g cm}^{-2}$ and $\Sigma_d \sim 0.3 \text{ g cm}^{-2}$ in the northern regions, with results of $\Sigma_g \sim 0.2 \text{ g cm}^{-2}$ and $\Sigma_d \sim 0.01 \text{ g cm}^{-2}$ in the southern regions. The contrast along the Σ_g and Σ_d ridges are 5 and 33, respectively. The gas-to-dust ratio, $\text{G/D} \equiv \Sigma_g/\Sigma_d$, is derived to vary smoothly in the azimuthal direction of the disk, where it is ~ 3 and ~ 20 in the northern and southern regions, respectively.
4. By using the results of Σ_g and Σ_d derived at the Σ_d ridge, we found that Σ_g varies approximately as $\Sigma_d^{0.47}$, or equivalently $\text{G/D} \propto \Sigma_d^{-0.53}$. This relation will be a critical test for future theoretical studies to understand the azimuthal-asymmetric disk structure.
5. Our results show that the Σ_d peak is slightly shifted ahead of the Σ_g , which is predicted

by theoretical studies of the trapping of dust by vortices of high gaseous pressures. The estimated dust size is $\gtrsim 5$ mm if $\chi(\text{C}^{18}\text{O}/\text{H}_2)$ in the disk is similar to the interstellar value.

6. The ^{13}CO $J = 1 - 0$ line emission in $\text{P.A.} = 200^\circ - 240^\circ$ is marginally optically thin, where we derive $N_{\text{tot}}(^{13}\text{CO})/N_{\text{tot}}(\text{C}^{18}\text{O}) = 9.99 \pm 1.67$; the value agrees with the interstellar abundance ratio $\chi(^{13}\text{CO}/\text{C}^{18}\text{O}) = 8.11 \pm 1.1$ within uncertainties.

Acknowledgments

This work was supported by JSPS KAKENHI Grant Numbers 17H01103 and 18H05441. This paper makes use of the following ALMA data: ADS/JAO.ALMA#2011.0.00318S and ADS/JAO.ALMA#2013.1.00670S. ALMA is a partnership of ESO (representing its member states), NSF (USA) and NINS (Japan), together with NRC (Canada), MOST and ASIAA (Taiwan), and KASI (Republic of Korea), in cooperation with the Republic of Chile. The Joint ALMA Observatory is operated by ESO, AUI/NRAO and NAOJ.

Appendix 1 Channel maps of ^{13}CO $J = 1 - 0$ and C^{18}O $J = 1 - 0$

Figure 11 shows the channel maps of ^{13}CO and C^{18}O line emission from which the moment maps shown in figures 3 and 5 are created. When creating the moment maps, we first mask out the regions where Keplerian motion of the disk is not expected in the velocity channels (Salinas et al. 2017; Ansdell et al. 2018), and the emission below 3.5σ in the unmasked region is then clipped. We adopt a stellar mass of $M_* = 2.4 M_\odot$ and a disk inclination of $i = 27^\circ$ when creating the Keplerian mask.

Appendix 2 Two-layer disk model

To evaluate the uncertainties of G/D and the exponent p , we here adopt a two-layer disk model when deriving the surface densities, where the temperature of gas and dust particles are different. The gas temperature T_g is assumed to be the same as the brightness temperature at the peak T_B of ^{13}CO $J = 3 - 2$ including the continuum emission, as shown in figure 4(d). The dust temperature T_d , on the other hand, is simply taken to be 80% of the gas temperature across the map; this physical condition mimics the effect of dust sedimentation. The 20% temperature drop results in a peak $T_d \approx 29$ K in the dust temperature field. Indeed, this agrees with the peak dust temperature derived by Casassus et al. (2015) using the continuum observations at Bands 7 and 9, and therefore it is a reasonable estimate for the dust temperature.

Figure 12 shows the optical depth of the continuum emission at 98.5 GHz and 336 GHz, and the dust opacity spectral index β derived from the two-layer disk model; they are larger

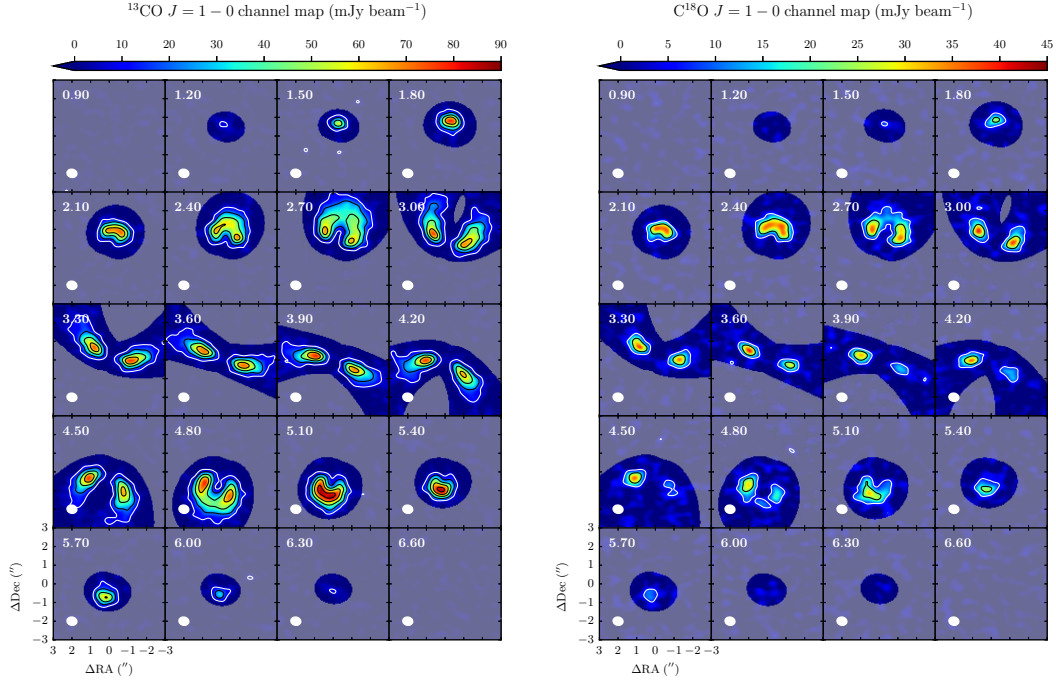


Fig. 11: The velocity channel maps of the $^{13}\text{CO } J = 1 - 0$ (left panel) and $\text{C}^{18}\text{O } J = 1 - 0$ (right panel) line emission. The velocity (in units of km s^{-1}) is written in the top left corner in each channel map. The white ellipse in the bottom left indicates the synthesized beam, which is identical to that of the 98.5 GHz continuum image shown in figure 1 ($0''.54 \times 0''.44$, P.A. = 78.1°). The white contour denotes the $3.5\sigma = 7 \text{ mJy beam}^{-1}$ and the black contours are drawn at (20, 40, 60, 80) mJy beam^{-1} . The white shaded regions denote the Keplerian masks used to create the moment maps in figures 3 and 5.

than those derived from the one-layer disk model due to the lower temperature. In addition, the larger β results in a smaller dust opacity κ_d , where it is smaller than that of the one-layer disk model by $\approx 10\%$ in the disk southern region and by $\approx 30\% - 50\%$ in the dust concentrated northern region.

The radiative transfer for the gas molecular line in the two-layer disk model reads

$$\begin{aligned}
 I_{\text{g+d}} = & [B_\nu(T_g) - B_\nu(T_{\text{bg}})] [1 - \exp(-\tau_g/2)] \\
 & + [B_\nu(T_d) - B_\nu(T_{\text{bg}})] [1 - \exp(-\tau_g)] \exp(-\tau_g/2) \\
 & + [B_\nu(T_g) - B_\nu(T_{\text{bg}})] [1 - \exp(-\tau_g/2)] \exp(-\tau_g/2 - \tau_d),
 \end{aligned}
 \tag{A1}$$

where $I_{\text{g+d}}$ denotes the line emission including the continuum emission (Nomura et al. 2016). In the line of sight, the first term accounts for the line emission from the disk atmosphere at

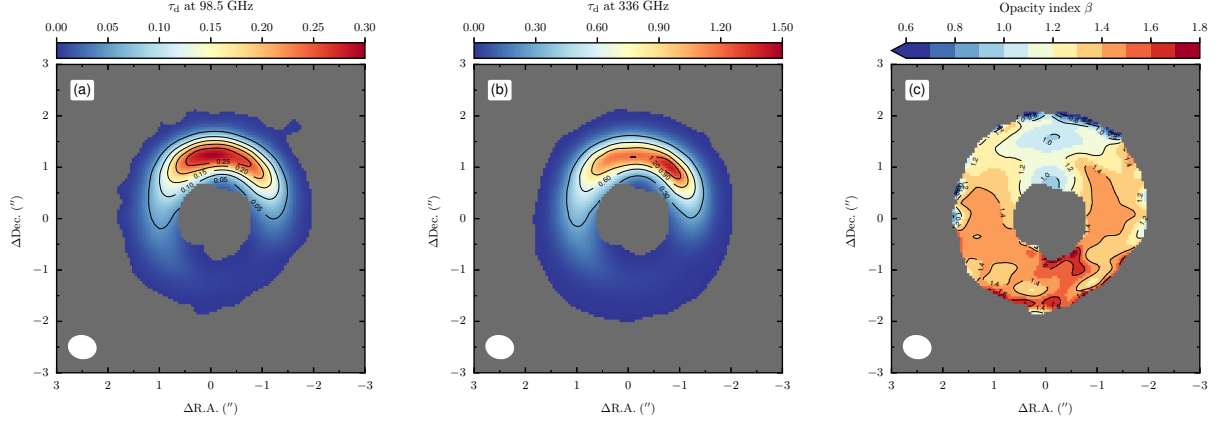


Fig. 12: Similar to figure 7, for the results derived from the two-layer disk model.

the front side, the second term the dust emission in the disk midplane, while the last term the line emission from the back side that will propagate through the disk midplane and the front atmosphere.

Figure 13 shows the results derived from this two-layer disk model. We mask out the disk inner region in which the disk temperature is lower than 24 K, i.e., 80% of the temperature criteria used to mask out the disk inner region in the one-layer disk model (Section 4). The overall distributions of Σ_g , Σ_d , and G/D are similar to the one-layer disk model; due to the lower κ_d , however, in the northern region Σ_d is derived to be twice as high as that in the one-layer disk model, and therefore the G/D distribution is derived to be lower. Figure 14(a) shows the correlation between Σ_g and Σ_d . Similar to figure 9(a) we find a power law with an exponent $p = 0.44$ to be a good fit to the results. The derived value of exponent p is consistent with that of the one-layer disk model despite the different temperature assumption between these two disk models. Figure 14(b) is analogous to figure 9(b), where the derived values of p are also consistent between the two models.

Appendix 3 Mock-up dust continuum image at 700 GHz

By using the dust surface density Σ_d distribution derived from the one layer-disk model (figure 8a), we create a mock-up image at 700 GHz to compare with the continuum observations at the same frequency reported by Casassus et al. (2015). We use the same temperature distribution, i.e., the peak T_B of $^{13}\text{CO } J = 3 - 2$ including the continuum (figure 4d) as the disk temperature and the β distribution (figure 7c) to calculate the dust opacity κ_d at 700 GHz (Equation 5). The radiative transfer follows Equation (4). Figure 15 shows the mock-up image. Though

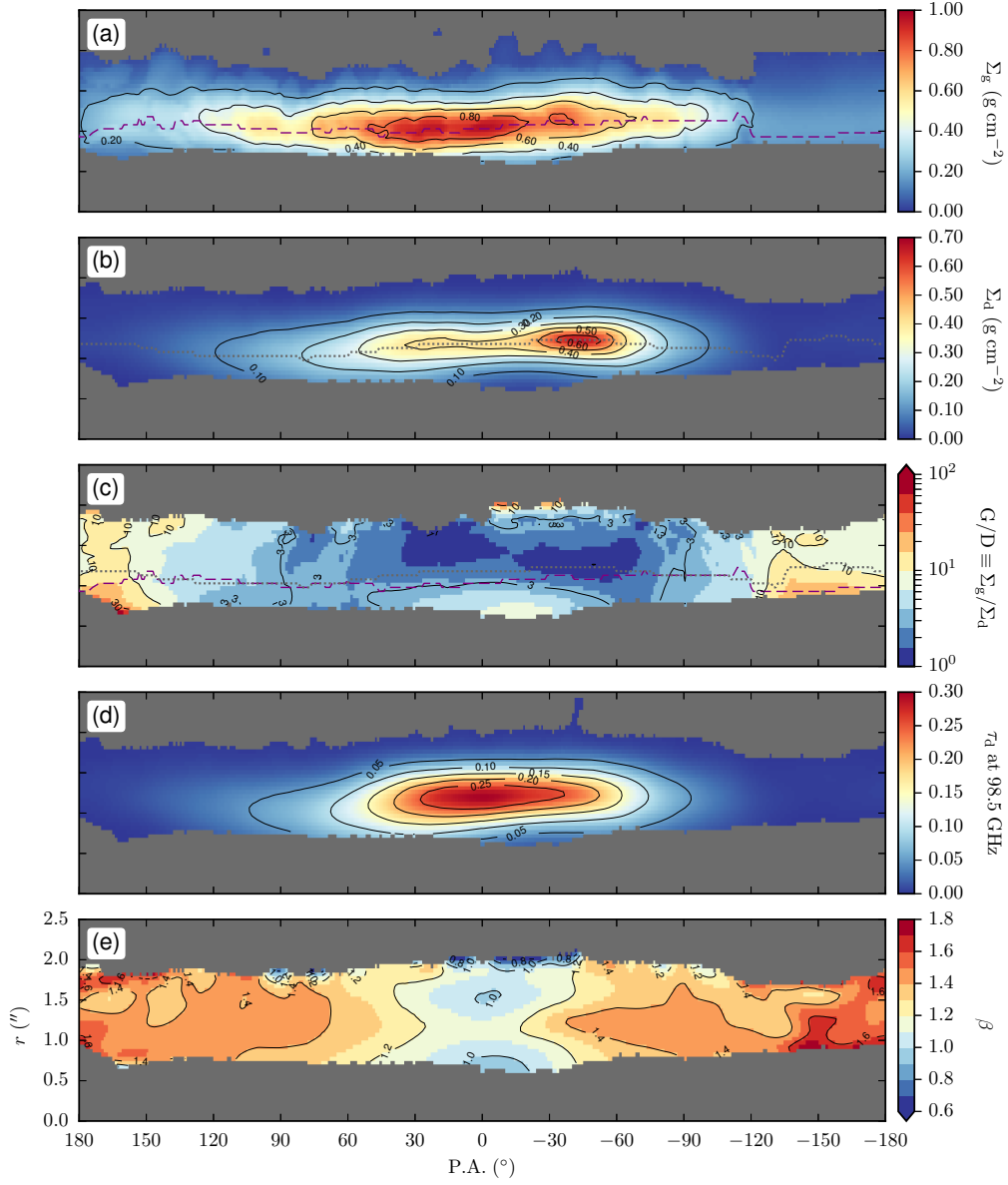


Fig. 13: Similar to figure 10, but the results are derived from the two-layer disk model. Note that only the color scale range of (b) is twice wider than that in figure 10(b), while the others have the same scaling range.

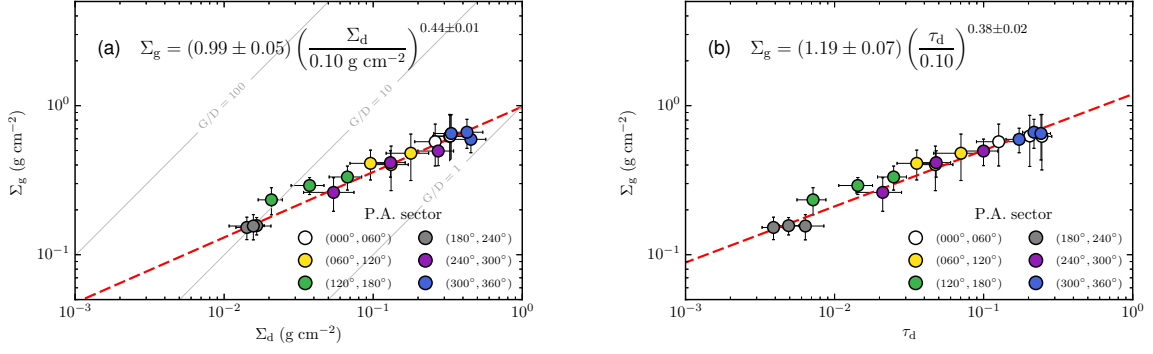


Fig. 14: Similar to figure 9, for the results derived from the two-layer disk model.

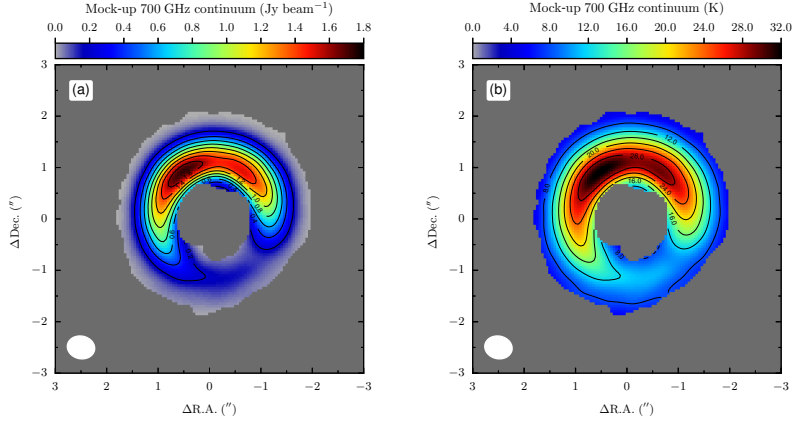


Fig. 15: The mock-up dust continuum image at 700 GHz. Panels (a) and (b) present the continuum emission in units of Jy beam^{-1} and K, respectively. The ellipse in the lower left corner indicates the beam size ($0''.54 \times 0''.44$, P.A. = 78°) of the Band 3 and Band 7 observations, which are used to derive the Σ_d distribution.

the beam size is larger than that of the image obtained by Casassus et al. (2015), our mock up image successfully reproduces the observed intensity distribution, in which there are two emission peaks and the northwestern one is brighter (because the temperature in this region is higher). This comparison shows that the disk parameters estimated from Bands 3 and 7 are reasonable.

References

- ALMA Partnership, Brogan, C. L., Pérez, L. M., et al. 2015, *ApJL*, 808, L3
 Andrews, S. M., Huang, J., Pérez, L. M., et al. 2018, *ApJL*, 869, L41
 Ansdell, M., Williams, J. P., Trapman, L., et al. 2018, *ApJ*, 859, 21

- Armitage, P. J. 2010, *Astrophysics of Planet Formation*
- Arun, R., Mathew, B., Manoj, P., et al. 2019, *AJ*, 157, 159
- Avenhaus, H., Quanz, S. P., Schmid, H. M., et al. 2014, *ApJ*, 781, 87
- Barge, P., & Sommeria, J. 1995, *A&A*, 295, L1
- Baruteau, C., & Zhu, Z. 2016, *MNRAS*, 458, 3927
- Beckwith, S. V. W., & Sargent, A. I. 1991, *ApJ*, 381, 250
- Beckwith, S. V. W., Sargent, A. I., Chini, R. S., & Guesten, R. 1990, *AJ*, 99, 924
- Bergin, E. A., Cleeves, L. I., Gorti, U., et al. 2013, *Nature*, 493, 644
- Biller, B., Lacour, S., Juhász, A., et al. 2012, *ApJL*, 753, L38
- Birnstiel, T., Dullemond, C. P., & Pinilla, P. 2013, *A&A*, 550, L8
- Birnstiel, T., Dullemond, C. P., Zhu, Z., et al. 2018, *ApJL*, 869, L45
- Boehler, Y., Weaver, E., Isella, A., et al. 2017, *ApJ*, 840, 60
- Boehler, Y., Ricci, L., Weaver, E., et al. 2018, *ApJ*, 853, 162
- Casassus, S., van der Plas, G., M, S. P., et al. 2013, *Nature*, 493, 191
- Casassus, S., Wright, C. M., Marino, S., et al. 2015, *ApJ*, 812, 126
- Cazzoletti, P., van Dishoeck, E. F., Pinilla, P., et al. 2018, *A&A*, 619, A161
- Close, L. M., Follette, K. B., Males, J. R., et al. 2014, *ApJL*, 781, L30
- Dipierro, G., Laibe, G., Alexander, R., & Hutchison, M. 2018, *MNRAS*, 479, 4187
- Dipierro, G., Laibe, G., Price, D. J., & Lodato, G. 2016, *MNRAS*, 459, L1
- Dominik, C., Blum, J., Cuzzi, J. N., & Wurm, G. 2007, *Protostars and Planets V*, 783
- Dong, R., Li, S., Chiang, E., & Li, H. 2017, *ApJ*, 843, 127
- Draine, B. T. 2006, *ApJ*, 636, 1114
- van der Plas, G., Casassus, S., Ménard, F., et al. 2014, *ApJL*, 792, L25
- Fu, W., Li, H., Lubow, S., Li, S., & Liang, E. 2014, *ApJL*, 795, L39
- Fujiwara, H., Honda, M., Kataza, H., et al. 2006, *ApJL*, 644, L133
- Fukagawa, M., Tamura, M., Itoh, Y., et al. 2006, *ApJL*, 636, L153
- Fukagawa, M., Tsukagoshi, T., Momose, M., et al. 2013, *PASJ*, 65, L14
- Gaia Collaboration, Brown, A. G. A., Vallenari, A., et al. 2016, *A&A*, 595, A2
- Gaia Collaboration, Prusti, T., de Bruijne, J. H. J., et al. 2016, *A&A*, 595, A1
- Gonzalez, J.-F., Laibe, G., & Maddison, S. T. 2017, *MNRAS*, 467, 1984
- Gorti, U., Hollenbach, D., & Dullemond, C. P. 2015, *ApJ*, 804, 29
- Hayashi, C. 1981, *Progress of Theoretical Physics Supplement*, 70, 35
- Isella, A., Pérez, L. M., Carpenter, J. M., et al. 2013, *ApJ*, 775, 30
- Kanagawa, K. D., Muto, T., Tanaka, H., et al. 2016, *PASJ*, 68, 43

- Kataoka, A., Okuzumi, S., Tanaka, H., & Nomura, H. 2014, *A&A*, 568, A42
- Klahr, H. H., & Henning, T. 1997, *Icarus*, 128, 213
- Lacour, S., Biller, B., Cheetham, A., et al. 2016, *A&A*, 590, A90
- Lambrechts, M., & Johansen, A. 2012, *A&A*, 544, A32
- Lyra, W., Raettig, N., & Klahr, H. 2018, *Research Notes of the American Astronomical Society*, 2, 195
- Malfait, K., Bogaert, E., & Waelkens, C. 1998, *A&A*, 331, 211
- Mangum, J. G., & Shirley, Y. L. 2015, *PASP*, 127, 266
- Marino, S., Perez, S., & Casassus, S. 2015, *ApJL*, 798, L44
- McClure, M. K., Bergin, E. A., Cleaves, L. I., et al. 2016, *ApJ*, 831, 167
- Mendigutía, I., Fairlamb, J., Montesinos, B., et al. 2014, *ApJ*, 790, 21
- Miyake, K., & Nakagawa, Y. 1993, *Icarus*, 106, 20
- Miotello, A., Bruderer, S., & van Dishoeck, E. F. 2014, *A&A*, 572, A96
- Miotello, A., van Dishoeck, E. F., Kama, M., et al. 2016, *A&A*, 594, A85
- Miotello, A., van Dishoeck, E. F., Williams, J. P., et al. 2017, *A&A*, 599, A113
- Molyarova, T., Akimkin, V., Semenov, D., et al. 2017, *ApJ*, 849, 130
- Muto, T., Tsukagoshi, T., Momose, M., et al. 2015, *PASJ*, 67, 122
- Nomura, H., Tsukagoshi, T., Kawabe, R., et al. 2016, *ApJL*, 819, L7
- Ohashi, S., Kataoka, A., Nagai, H., et al. 2018, *ApJ*, 864, 81
- Okuzumi, S., Momose, M., Sirono, S.-i., Kobayashi, H., & Tanaka, H. 2016, *ApJ*, 821, 82
- Pérez, L. M., Isella, A., Carpenter, J. M., & Chandler, C. J. 2014, *ApJL*, 783, L13
- Perez, S., Casassus, S., Ménard, F., et al. 2015, *ApJ*, 798, 85
- Pinte, C., Dent, W. R. F., Ménard, F., et al. 2016, *ApJ*, 816, 25
- Planck Collaboration, Ade, P. A. R., Aghanim, N., et al. 2014, *A&A*, 564, A45
- Price, D. J., Cuello, N., Pinte, C., et al. 2018, *MNRAS*, 477, 1270
- Qi, C., D'Alessio, P., Öberg, K. I., et al. 2011, *ApJ*, 740, 84
- Raettig, N., Klahr, H., & Lyra, W. 2015, *ApJ*, 804, 35
- Ragusa, E., Dipierro, G., Lodato, G., et al. 2017, *MNRAS*, 464, 1449
- Rice, W. K. M., Armitage, P. J., Wood, K., & Lodato, G. 2006, *MNRAS*, 373, 1619
- Salinas, V. N., Hogerheijde, M. R., Mathews, G. S., et al. 2017, *A&A*, 606, A125
- Shimajiri, Y., Kitamura, Y., Saito, M., et al. 2014, *A&A*, 564, A68
- Soon, K.-L., Hanawa, T., Muto, T., Tsukagoshi, T., & Momose, M. 2017, *PASJ*, 69, 34
- Takahashi, S. Z., & Inutsuka, S.-i. 2014, *ApJ*, 794, 55
- Takahashi, S. Z., & Inutsuka, S.-i. 2016, *AJ*, 152, 184

- Tazaki, R., & Tanaka, H. 2018, *ApJ*, 860, 79
- Tazaki, R., Tanaka, H., Okuzumi, S., Kataoka, A., & Nomura, H. 2016, *ApJ*, 823, 70
- Tsukagoshi, T., Momose, M., Kitamura, Y., et al. 2019, *ApJ*, 871, 5
- van den Ancker, M. E., de Winter, D., & Tjin A Djie, H. R. E. 1998, *A&A*, 330, 145
- van der Marel, N., van Dishoeck, E. F., Bruderer, S., et al. 2016, *A&A*, 585, A58
- van der Marel, N., van Dishoeck, E. F., Bruderer, S., et al. 2013, *Science*, 340, 1199
- van der Plas, G., Casassus, S., Ménard, F., et al. 2014, *ApJL*, 792, L25
- Verhoeff, A. P., Min, M., Pantin, E., et al. 2011, *A&A*, 528, A91
- Weaver, E., Isella, A., & Boehler, Y. 2018, *ApJ*, 853, 113
- Weidenschilling, S. J. 1977, *Ap&SS*, 51, 153
- Weidenschilling, S. J. 1977, *MNRAS*, 180, 57
- Wilson, T. L. 1999, *Reports on Progress in Physics*, 62, 143
- Yu, M., Willacy, K., Dodson-Robinson, S. E., Turner, N. J., & Evans, N. J., II 2016, *ApJ*, 822, 53
- Yu, M., Evans, N. J., II, Dodson-Robinson, S. E., Willacy, K., & Turner, N. J. 2017, *ApJ*, 841, 39
- Zhang, K., Blake, G. A., & Bergin, E. A. 2015, *ApJL*, 806, L7
- Zhu, Z., & Baruteau, C. 2016, *MNRAS*, 458, 3918